arXiv:1704.01085v1 [cs.CV] 4 Apr 2017

Deep Depth From Focus

Caner Hazirbas
hazirbas@cs.tum.edu

Laura Leal-Taixé
leal.taixe@tum.de

Daniel Cremers
cremers@tum.de

Technical University of Munich

Abstract

Depth from Focus (DFF) is one of the classical ill-posed inverse problems in computer vision. Most approaches recover the depth at each pixel based on the focal setting which exhibits maximal sharpness. Yet, it is not obvious how to reliably estimate the sharpness level, particularly in low-textured areas. In this paper, we propose 'Deep Depth From Focus (DDFF)' as the first end-to-end learning approach to this problem. Towards this goal, we create a novel real-scene indoor benchmark composed of 4D light-field images obtained from a plenoptic camera and ground truth depth obtained from a registered RGB-D sensor. Compared to existing benchmarks our dataset is 30 times larger, enabling the use of machine learning for this inverse problem. We compare our results with state-of-the-art DFF methods and we also analyze the effect of several key deep architectural components. These experiments show that DDFFNet achieves state-of-the-art performance in all scenes, reducing depth error by more than 70% wrt classic DFF methods.

1. Introduction

The goal of *depth from focus* (DFF) is to reconstruct a pixel-accurate disparity map given a stack of images with gradually changing optical focus. The key observation is that a pixel's sharpness is maximal when the object it belongs to is in focus. Hence, most methods determine the depth at each pixel by finding the focal distance at which the contrast measure is maximal. Nonetheless, DFF is an ill-posed problem, since this assumption does not hold for all cases, especially for textureless surfaces where sharpness cannot be determined. This is why most methods rely on strong regularization to obtain meaningful depth maps which in turn leads to an often oversmoothed output.

While spatial smoothness is a rather primitive prior for depth reconstruction, with the advent of Convolutional Neural Networks (CNNs) we now have an alternative technique to resolve classical ill-posed problems such as semantic segmentation [29, 5, 16, 35] or optical flow estimation [10, 34]. The underlying expectation is that the rather naive and generic spatial smoothness assumption used in variational inference techniques is replaced with a more object-specific prior knowledge absorbed through huge amounts of training data.

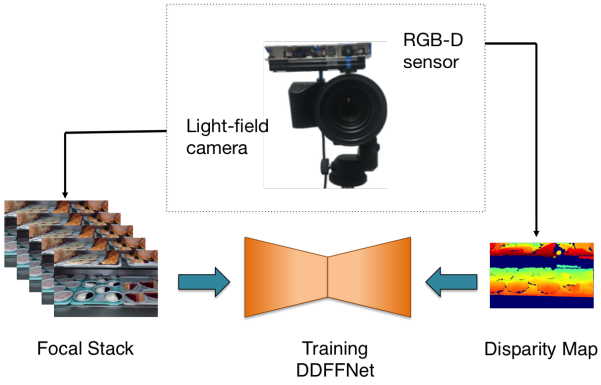

Figure 1. **Experimental setup.** We place an RGB-D sensor on top of a plenoptic camera in order to capture calibrated ground truth depth maps and light-field images from which we then create focal stacks. These two inputs will be used to train *DDFNet*.

A big strength of CNNs is their ability to extract meaningful image features, and correlate pixel information via convolutions. Our intuition is that a network will be able to find the image in the focal stack at which a pixel is maximally sharp, thereby correlating focus and depth. We therefore propose to tackle the task of Depth From Focus using end-to-end-learning. To that end, we create the first DFF dataset with real-world scenes and ground truth measured depth. Using this new dataset, we aim at performing end-to-end learning of the disparity given a focal stack.

1.1. Contribution

In this paper, we present *Deep Depth From Focus Network* (DDFFNet), an auto-encoder-style Convolutional Neural Network that outputs a disparity map from a focal

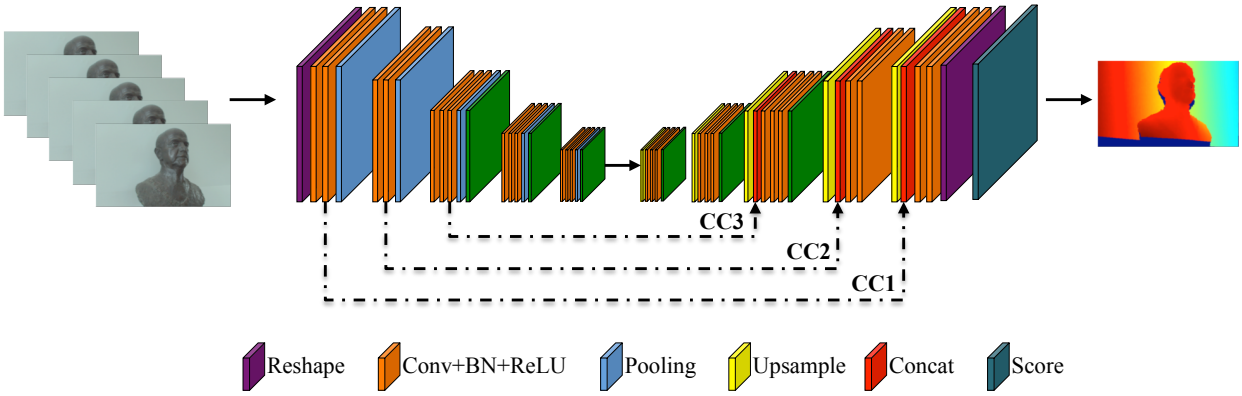

Figure 2. **DDFFNet.** Proposed encoder-style architecture that takes in a focal stack and produces a disparity map. We present several architectural modifications, namely CC connections, Upsample, *i.e*. Unpool, BL and UpConv (check the text for details).

stack. For this purpose, we create a dataset composed of 12 indoor scenes, consist of in total of 720 light-field images using a plenoptic camera, *i.e*. Lytro ILLUM. Ground truth depth is obtained from an RGB-D sensor which is calibrated to the light-field camera. To the best of our knowledge, this is the largest dataset with ground truth for the problem of DFF. We experimentally show that this amount of data is enough to successfully fine-tune a network. We compare our results with state-of-the-art DFF methods and provide a comprehensive study on the impact of different variations of the encoder-decoder type of network.
The contribution of this paper is three-fold:

- We propose DDFFNet, the first end-to-end learning method to compute depth maps from focal stacks.
- We introduce DDFF 12-Scene: a dataset with 720 light-field images and registered ground truth depth maps recorded with an RGB-D sensor. We show that this data is enough to fine-tune a network for the task of DFF.
- We compare several state-of-the-art methods for DFF, as well as several variations of the encoder-decoder architecture, and show that our method outperforms all of them by a large margin. It computes depth maps in 0.6 seconds on an NVidia Pascal Titan X GPU.

1.2. Related work

Depth from Focus or Shape from Focus. Conventional methods aim at determining the depth of a pixel by measuring its sharpness or focus at different images of the focal stack [39]. Developing a discriminative measure for sharpness is non trivial, we refer the reader to [39] for a overview. Other works aim at filtering the constrast coefficients before determining depth values by *i.e*., windowed averaging [44] or non-linear filtering [31]. Another popular approach to obtain consistent results is to use total variation regularization. [30] proposed the first variational approach to tackle DFF, while [32] defines an objective function composed of a smooth but nonconvex data term with a non-smooth but convex regularizer to obtain a robust (noise-free) depth map. Suwajanakorn *et al*. [43] computes DFF on mobile devices, focusing on compensating the motion between images of the focal stack. This results in a very involved model, that depends on optical flow results, and that takes 20 minutes to obtain a depth map. Aforementioned methods heavily rely on priors/regularizers to increase the robustness of the algorithm, meaning their models may not generalize to all scenes. Interestingly, shape from focus was already tackled using neural networks in 1999 [4], showing their potential with synthetic toy experiments. The increasing power of deep architectures makes it now possible to move towards estimating depth of real-world scenarios.
Plenoptic or light-field cameras. A light-field or plenoptic camera capture angular and spatial information on the distribution of light rays in space. In a single photographic exposure, these cameras are able to obtain multi-view images of a scene. The concept was first proposed in [3], and has recently gained interest from the computer vision community. These cameras have evolved from bulky devices [46] to hand-held cameras based on micro-lens arrays [33]. Several works focus on the calibration of these devices, either by using raw images and line features [6] or by decoding 2D lenslet images into 4D light-fields [8]. A detailed analysis of the calibration pipeline is detailed in [7]. Light-field cameras are particularly interesting since depth and all-in-focus images can be computed directly from the 4D light-field [21, 38, 26]. Furthermore, focal stacks, *i.e*., images taken at different optical focuses, can be obtained from plenoptic cameras with a single photographic exposure. For this reason, we choose to capture our training dataset using these cameras, though any normal camera that captures im-

ages at different optical focuses can be used at test time.

To the best of our knowledge, there are only two light-field datasets with ground truth depth maps [45, 19]. While [45] provides 7 synthetic and only 6 real-scene light-fields, [19] generates a hand-crafted synthetic light-field benchmark composed of only 24 samples with ground truth disparity maps. Our dataset, is 30 times larger, composed of 12 indoor scenes, in total of 720 light-field samples with registered ground truth depth obtained from an RGB-sensor, ranging from 0.5 to 7m. In this work, we show that our data is enough to fine-tune a network for the specific task of predicting depth from focus.

Deep learning. Deep learning has had a large impact in computer vision since showing their excellent performance in the task of image clasification [24, 42, 18]. A big part of their success has been the creation of very large annotated datasets such as ImageNet [40]. Of course, this can also be seen as a disadvantage, since creating such datasets with millions of annotations for each task would be impractical. Numerous recent works have shown that networks pre-trained on large datasets for seemingly unrelated tasks like image classification, can easily be fine-tuned to a new task for which there exists only a fairly small training dataset. This paradigm has been successfully applied to object detection [15], pixel-wise semantic segmentation [29, 5, 22, 16, 35], depth and normal estimation [25] or single image-based 3D localization [23], to name a few. Another alternative is to generate synthetic data to train very large networks, *i.e*. for optical flow estimation [10, 34]. Using synthetic data for training is not guaranteed to work, since the training data often does not capture the real challenge and noise distribution of real data. Several works use external sources of information to produce ground truth. [13] use sparse multi-view reconstruction results to train a CNNs to predict surface normals, which are in turned used to improve the reconstruction. In [14], authors aim at predicting depth from a single image, but create ground truth depth data from matching stereo images. We propose to use an RGB-D sensor that can be registered to our light-field camera to obtain the ground truth depth map. Even though an RGB-D sensor is not noise-free, we show that the network can properly learn to predict depth from focus even from imperfect data. We also use the paradigm of finetuning a pre-trained network and show that this works even if the tasks of image classification and DFF seem to be relatively unrelated.

2. DDFF 12-Scene Benchmark

In this section we present our indoor DDFF 12-Scenes dataset for *Depth From Focus*. This dataset is used for the training and evaluation of the proposed and several state-of-the-art methods. We first give the details on how we generate our data, namely the focal stack and ground truth depth maps.

Light-field imaging. With light-field imaging technology, the original focus of the camera can be altered after the image is taken. Following this, we use a commercially available light-field camera, *i.e*. Lytro ILLUM [1], to collect data and then generate focal stacks. Plenoptic cameras capture a 4D light-field $L(u, v, x, y)$ which stores the light rays that intersect the image plane Ω at (x, y) and the focus or camera plane Π at (u, v). The pixel intensity $I(x, y)$ is then:

$$I(x,y) = \int_u \int_v L(u,v,x,y) \;\; \partial u \, \partial v, \tag{1}$$

Refocusing on an image corresponds to shifting and summing all sub-apertures, $I_{(u,v)}(x, y)$. Given the amount of shift, pixel intensities of a refocused image are computed as follows [9]:

$$I'(x,y) = \int_u \int_v L(u,v,x+\Delta_x(u), y+\Delta_y(v)) \, \partial u \, \partial v. \tag{2}$$

The shift (Δ_u, Δ_v) of each sub-aperture uv can be physically determined given an arbitrary depth Z in m, which the camera is in-focus:

$$\begin{pmatrix} \Delta_x(u) \\ \Delta_y(v) \end{pmatrix} = \underbrace{\frac{\text{baseline} \cdot f}{Z}}_{\text{disparity}} \cdot \begin{pmatrix} u_{center} - u \\ v_{center} - v \end{pmatrix}, \tag{3}$$

where the baseline is the distance between adjacent sub-apertures in meter/pixel, f is the focal length of microlenses in pixels and $(u \;\; v)^T$ indicates the spatial position of the sub-aperture in the Π plane in pixel. Although shifting can be performed using bilinear or bicubic interpolation, Lytro camera has a very narrow baseline and computed disparities are below 1 pixel. Therefore standard interpolation algorithms fail at preserving the sharpness of the refocused pixels. To be able to perform subpixel accurate focusing on the images, following [21] we use the *phase shift algorithm* to observe the impact of subpixel shifts on the images:

$$\mathcal{F}\{I'(x + \Delta_x(u))\} = \mathcal{F}\{I(x)\} \cdot \exp^{2\pi i \Delta_x(u)}, \tag{4}$$

where $\mathcal{F}\{\cdot\}$ is the 2D discrete Fourier transform.

We generate the focal stacks with a given disparity range, for which the focus shift on the images is clearly observable from close objects to far ones present in our dataset. Disparity values used in refocusing Equation (3) are sampled linearly in the given interval for a stack size of S, meaning that the focus plane equally shifts in-between the refocused images. Example refocused images for disparity $\in \{0.28, 0.17, 0.02\}$ are shown in Figure 3. Note, that we chose to use a light-field camera since it is easy to obtain a focal stack from it. Nonetheless, at test time, any

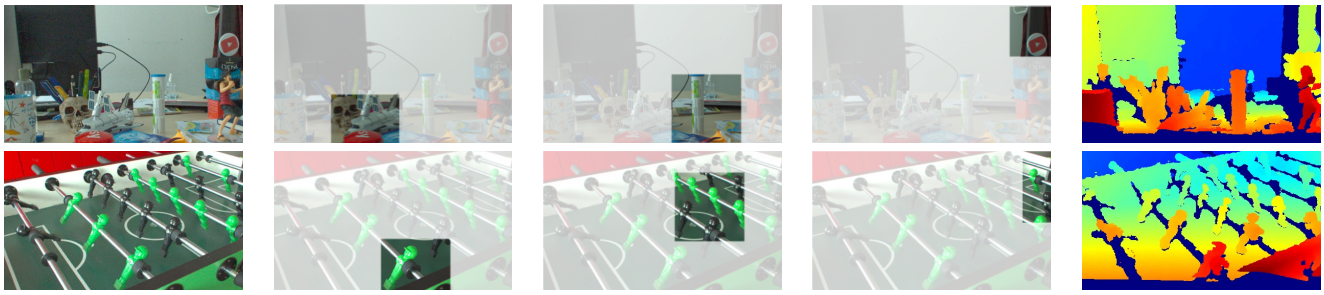

Figure 3. **Example refocused images.** *First column:* Center subaperture image. *Last column:* ground truth disparity maps from the RGB-D sensor. *Middle columns:* Refocused images for varying disparity values in pixels, regions in focus are highlighted. Best viewed in color.

Table 1. Estimated intrinsic parameters of the Lytro ILLUM. f_* and c_* are respectively the focal length ($f = f_x = f_y$) and optical center of the microlenses in pixels. Baseline is the distance between two adjacent subapertures in meter/pixel.

f	c_x	c_y	baseline
521.4	285.11	187.83	27e−5

imaging device could be used to take images at different optical focus.

Light-field camera calibration. For consistent capturing over all scenes, we fix the focal length of the main lens to $f = 9.5mm$ and lock the zoom. To increase the refocusable range of the camera, we use the *hyperfocal mode* (see [1] for details), in order to increase the refocusable range. Theoretically, we can then refocus from $27cm$ distance to infinity. We set the white-balancing, ISO and shutter speed settings to *auto* mode. In order to estimate the intrinsic parameters of the light-field camera, we use the calibration toolbox by Bok *et al*. [6] with a chessboard pattern composed of $26.25mm$ length squares. The radius of each microlens is set to 7 pixels as suggest in [6].

We can generate 9×9 undistorted subapertures, each of which has 383×552 image resolution. Estimated intrinsic parameters of the microlenses are given in Table 1. All estimated parameters will be included in the benchmark.

Ground truth depth maps from an RGB-D sensor. Along with the light-field images, we also provide ground truth depth maps. To this end, we use an RGB-D structure sensor, *i.e*. ASUS Xtion PRO LIVE, and mount it on the hot shoe of the light-field camera (see Figure 1). Since we only need the infrared camera of the RGB-D sensor, we align the main lens of Lytro ILLUM to the infrared image sensor as close as possible for a larger overlap on the field of views of both cameras. We save the 480×640 resolution depth maps in millimeters. RGB-D sensors are not accurate on light-reflecting surfaces and might even produce large amount of invalid/missing measurements. In order to reduce the number of missing values, we take nine consecutive frames and save the median depth of each pixel during recording/capturing.

Stereo camera calibration. We perform mono and stereo camera calibration to estimate the relative pose of the depth sensor with respect to the light-field camera. To this end, we use publicly available *Camera Calibration Toolbox for Matlab*[1]. We use the same calibration pattern as for the light-field calibration. Stereo calibration is performed between the center subaperture $(uv)^T = (55)^T$ and the infrared camera image. While we fix the intrinsics of the light-field camera as given in Table 1, depth sensor is calibrated only for intrinsic parameters (no distortion). After the calibration procedure, we register the depth maps onto the center subapertures images. As one can observe in the examples in Figure 3, due to the RGB-D sensor noise and the calibration procedure, some pixels around object boundaries do not contain depth measurements (represented in dark blue). Recorded depth maps can be improved further for a better domain adaptation [28, 37, 36, 41]. We leave the possible improvements as a future work. We convert depth to disparity in order to generalize the method to different camera inputs.

DDFF 12-Scene benchmark. We collect the dataset in twelve different indoor environments: *glassroom, kitchen, office41, seminar room, social corner, student laboratory, cafeteria, library, locker room, magistrale, office44* and *spencer laboratory*. First six scenes are composed of 100 and the latter six scenes are composed of 20 light-field images and depth pairs. Example center subaperture images for *office41* and *locker room* scenes and their corresponding disparity maps are shown in Figure 3. Our scenes have at most 0.5 pixel disparity while the amount of measured

[1] www.vision.caltech.edu/bouguetj/calib_doc/

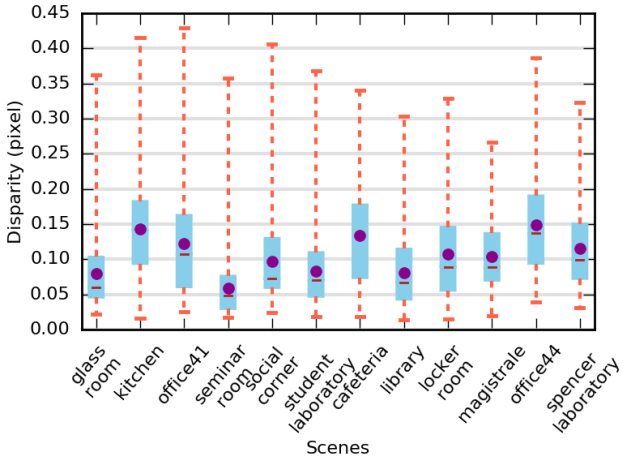

Figure 4. **Whisker diagram of the disparity distribution for each scene.** Circle and red line demonstrate the mean and median, respectively. While the minimum disparity is around 0.015 pixels (bottom orange lines), maximum disparity is less than 0.5 pixels (top orange lines).

disparity gradually decreases towards far distances. Figure 4 plots the Whisker diagrams for each scene. Since the dataset consists mainly of indoor scenes, flat surfaces (wall, desk), textureless objects (monitor, door, cabinet) and light-reflecting materials (screen, windows) are often present. Our dataset is therefore more challenging and 30 times larger than previous synthetic datasets [45, 19].

DDFF 12-Scene dataset, consisting of the light-field images, generated focal stacks, registered depth maps and the source code of our method will be publicly available on [2].

3. Depth from Focus using Convolutional Neural Networks

This section describes our method for depth reconstruction from a focus stack. We formulate the problem as a minimization of a regression function, which is an end-to-end trained convolutional neural network.

Let be $\mathcal{S}$ is a focal stack consists of S refocused images $I \in \mathbb{R}^{H\times W\times C}$ and the corresponding target disparity map $D \in \mathbb{R}^{H\times W}$. We minimize the least square error between the estimated disparity $f(\mathcal{S})$ and the target D:

$$\mathcal{L} = \sum_{p}^{HW} \mathcal{M}(p) \cdot \left\| f_{\mathbf{W}}(\mathcal{S}, p) - D(p) \right\|_2^2 + \lambda \|\mathbf{W}\|_2^2 . \quad (5)$$

Loss function $\mathcal{L}$ is summed over all valid pixels p where $D(p) > 0$, indicated by the mask $\mathcal{M}$ and $f : \mathbb{R}^{S\times H\times W\times C} \rightarrow \mathbb{R}^{H\times W}$ is a convolutional neural network. Weights, $\mathbf{W}$, are penalized with L2-norm.

[2] https://vision.cs.tum.edu/data/datasets/ddff12scene

Network architecture. We propose an end-to-end trainable auto-encoder style convolutional neural network. CNNs designed for image classification are mostly encoder type networks which reduce the dimension of the input to a 1D vector [24, 42, 18]. These type of networks are very powerful at constructing descriptive hierarchical features later used for image classification. This is why for tasks which require a pixel-wise output, the encoder part is usually taken from these pre-trained networks [24, 42, 18] and a mirrored decoder part is created to upsample the output to image size. We follow this same paradigm of hierarchical feature learning for pixel-wise regression tasks [29, 35, 22, 10, 34] and design a convolutional auto-encoder network to generate a dense disparity map, as shown in Figure 2.

As a baseline for the encoder network, we use the VGG-16 net [42]. It consists of 13 convolutional layers, 5 poolings and 3 fully-connected layers. In order to reconstruct the input size, we remove the fully-connected layers and reconstruct the decoder part of the network by mirroring the encoder layers. We invert the 2×2 pooling operation with 4×4 upconvolution (deconvolution) [29] with a stride of 2 and initialize the weights of the upconvolution layers with bilinear interpolation, depicted as upsample in Figure 2. Similar to the encoder part, we use convolutions after upconvolution layers to further sharpen the activation results. To accelerate convergence, we add batch normalization [20] after each convolution and learn the scale and shift parameters during training. Batch normalization layers are followed by rectified linear unit (ReLU) activation. Moreover, after the 3rd, 4th and 5th poolings and before the corresponding upconvolutions, we apply dropout with 0.5 probability during training similar to [22]. In order to preserve the sharp object boundaries, we concatenate the feature maps of early convolutions `conv1_2`, `conv2_2`, `conv3_3` with the decoder feature maps: output of the convolutions are concatenated with the output of corresponding upconvolutions. Figure 2 demonstrates a sketch of our network.

We refer to this architecture as *DDFFNet*, and we propose to study the performance of several variants, as shown in Figure 2:

- *DDFFNet-Upconv*: In the decoder part, we keep the upconvolutions.
- *DDFFNet-Unpool:* Upconvolutions are replaced with 2×2 unpooling operation [11].
- *DDFFNet-BL:* Upconvolutions are replaced with 2×2 bilinear interpolation (upsampling).
- *DDFFNet-CCx:* Here we study the effect of several concatenation connections, designed to obtain sharper edges in the depth maps.

Network input. VGG-16 net takes the input size of $H \times W \times C$, precisely $224 \times 224 \times 3$. In contrast, we need to input the whole focal stack $\mathcal{S}$ into the network. Computing features per stack image I is a general way of incorporation sharpness into DFF approaches [32] and we make us of this intuition within our end-to-end trained CNN. Since the depth of a pixel is correlated with the sharpness level of that pixel and the convolutions are applied through input channels C, we consider the network as a feature extractor and therefore, we reshape our input to $(B \cdot S \times H \times W \times C)$ with a batch size of B. Hence, the network generates one feature map per image in the stack with a size of $(B \cdot S \times H \times W \times 1)$. In order to train the network end-to-end, we reshape the output features maps to $(B \times H \times W \times S)$ and apply 1×1 convolution as a regression layer through the stack (depicted as *Score* layer in Figure 2).

4. Experimental Evaluation

We evaluate our method on the DDFF 12-scene dataset proposed in Section 2. We first split the 12-scene into training and test sets. We use the six scenes, *i.e. cafeteria, library, locker room, magistrale, office44, spencer laboratory* for testing as these scenes have in total 120 focal stacks and are also a good representation of the whole benchmark, as shown in Figure 4. The other 6 scenes are then used for training with a total of 600 focal stacks.

4.1. Evaluation Metrics

Following [14, 12, 27, 19] we evaluate the resulting depth maps with six different error metrics:

- MSE : $\frac{1}{|\mathcal{M}|} \sum_{p \in \mathcal{M}} \left\| f(\mathcal{S}_p) - D_p \right\|_2^2$
- RMS : $\sqrt{\frac{1}{|\mathcal{M}|} \sum_{p \in \mathcal{M}} \left\| f(\mathcal{S}_p) - D_p \right\|_2^2}$
- log RMS : $\sqrt{\frac{1}{|\mathcal{M}|} \sum_{p \in \mathcal{M}} \left\| \log f(\mathcal{S}_p) - \log D_p \right\|_2^2}$
- Absolute relative : $\frac{1}{|\mathcal{M}|} \sum_{p \in \mathcal{M}} \frac{|f(\mathcal{S}_p) - D_p|}{D_p}$
- Squared relative : $\frac{1}{|\mathcal{M}|} \sum_{p \in \mathcal{M}} \frac{\left\| f(\mathcal{S}_p) - D_p \right\|_2^2}{D_p}$
- Accuracy: % of D_p s.t $\max\left(\frac{f(\mathcal{S}_p)}{D_p}, \frac{D_p}{f(\mathcal{S}_p)}\right) = \delta < thr$
- BadPix(τ): $\frac{|\{p \in \mathcal{M} : |f(\mathcal{S}_p) - D_p| > \tau\}|}{|\mathcal{M}|} \cdot 100$
- Bumpiness: $\frac{1}{|\mathcal{M}|} \sum_{p \in \mathcal{M}} \min(0.05, \|\mathrm{H}_{\Delta}(p)\|_F) \cdot 100$

where $\Delta = f(\mathcal{S}_p) - D_p$ and H is the Hessian matrix. The first five measures are standard error measures, therefore lower is better, while for the Accuracy measure higher is better. BadPix(τ) quantifies the number of wrong pixels with a given threshold τ, while Bumpiness metric focuses on the smoothness of the predicted depth maps [19].

4.2. Experimental setup

For our experiments, we generate the focal stacks for $S = 10$ with disparities linearly sampled in $[0.28, 0.02]$ pixel (equivalent to $= [0.5, 7]$ meters). We found this to be a good compromise between obtaining pixel sharpness at all depths and memory consumption and runtime, which heavily increases for larger focal stack without bringing improved depth accuracy.

DDFF 12-scene consists of 383×552 images, thus training on full resolution stacks is inefficient. One solution would be to downsample the images, however, interpolation could change the blur kernels, eventually affecting network performance. The solution we adopt is to train the network on $10 \times 224 \times 224 \times 3$ stack patches. To do so, we crop the training stacks and corresponding disparity maps with a patch size of 224 and a stride of 56, ensuring that cropped patches cover the whole image. Patches with more than 20% missing disparity values are removed from the training set. 20% of the training data is used for validation for model selection. At test time, results are computed on the full resolution 383×552 images.

Our method is implemented on Tensorflow [2] and all experiments are run on an NVidia Pascal Titan X GPU. The weights of the encoder part of the network are initialized from VGG-16 net, while both the convolution and batch normalization layers in the decoder part are initialized with variance scaling [17]. Networks are trained with Stochastic Gradient Descent using momentum. We used a batch size B of 2, learning rate of 0.001 and momentum decay of 0.9. Learning rate was reduced exponentially by a factor of 0.9 with a decay step of 4 epochs and we set the weight decay λ for convolution layers to 0.0005. Training set is shuffled in the beginning of each epoch.

4.3. Comparison to state-of-the-art

We compare our results with the state-of-the-art variational method, VDFF, in [32], using their GPU code[3]. We used the provided default parameters and ran the optimization for 600 iterations, since these delivered the best results for our dataset. The same focal stack is used for this method and our method. VDFF [32] outputs a real valued index map. Each pixel is assigned to one of the stack images, where the pixel is in focus. Therefore, we directly interpolate these indices to their corresponding disparity values and compute our metrics on the mapped disparity output.

Furthermore, we also compare with the depth map computed from the light-field directly by the Lytro toolbox [1].

[3] https://github.com/adrelino/variational-depth-from-focus

Table 2. **Quantitative results of the proposed method.** ***DDFFNet-CC3*** is the best depth from focus method and provides on-par results compared to Lytro, *i.e*. depth from light field. Metrics are computed on the predicted and the ground truth disparity images.

	Method	MSE ↓	RMS ↓	log RMS ↓	Abs. rel. ↓	Sqr. rel.↓	Accuracy δ=1.25 ↑	δ=1.25^2 ↑	δ=1.25^3 ↑	Bump. ↓
DDFFNet	Unpool	$2.4\,e^{-3}$	0.045	0.45	0.56	0.04	46.02	69.11	82.03	0.67
	BL	$2.8\,e^{-3}$	0.046	0.49	0.37	0.02	47.95	73.18	85.09	0.54
	UpConv	$2.7\,e^{-3}$	0.045	0.44	0.43	0.031	50.87	74.11	84.03	0.55
	CC1	$2.6\,e^{-3}$	0.047	0.47	0.54	0.040	43.85	68.93	81.29	0.76
	CC2	$2.5\,e^{-3}$	0.045	0.46	0.43	0.03	46.88	72.23	85.19	0.74
	CC3	$2.1\,e^{-3}$	0.041	0.41	0.35	0.02	46.91	74.29	87.03	0.59
	Lytro	$2.1\,e^{-3}$	0.040	0.31	0.26	0.01	55.65	82.00	93.09	1.017
	VDFF	$7.3\,e^{-3}$	0.080	1.39	0.62	0.05	8.42	19.95	32.68	0.79

Table 3. **Depth error in meters.** DDFFNet performs more accurate than other state-of-the-art methods.

	Lytro	VDFF	CC1	CC2	CC3
MSE	0.99	8.90	1.30	1.20	**0.98**
RMS	1.16	2.74	0.88	0.88	**0.81**

Table 4. **Runtime.** DDFFNet performs faster than other state-of-the-art methods.

	Method	Runtime (seconds)
DDFFNet	Unpool	**0.52**
	BL	**0.52**
	UpConv	0.62
	CC1	0.64
	CC2	0.66
	CC3	0.60
	VDFF	2.83
	Lytro	25.26 (CPU)

Although this method technically does not compute DFF, we still think it is a valuable baseline to show the accuracy that depth from light-field methods can achieve.

Lytro Toolbox predicts a depth in lambda units, thus the output is not directly comparable to our results. For this reason, we formulate the rescaling from Lytro depth to our ground truth as an optimization problem that finds a unique scaling factor k^*. To do so, we minimize the least squares error between the resulting depth $\tilde{Z}_p$ and the ground truth depth Z_p to find the best scaling factor k^*:

$$k^* = \arg\min_k \sum_p \|k \cdot \tilde{Z}_p - Z_p\|_2^2 \,, \tag{6}$$

where $k \in \mathbb{R}$. Note that this is the best possible mapping in terms of MSE to our ground truth depth maps provided that the focal stack has uniform focal change, therefore, we are not penalizing [1] during the conversion process. Evaluation metrics are then computed for $k^* \cdot \tilde{D}_p$ and D_p. We present the quantitative results in the lower part on Table 2.

4.4. Evaluation of the method

We first evaluate our architecture variations and present the evaluation metrics on Table 2. We test three upsampling layers, unpooling, upconvolution and bilinear interpolation. Even though Unpool has the lowest error, it creates artifacts in the output disparity map. BL, on the other hand, oversmooths the edges due to naive linear interpolation, which is why we choose to use UpConv for the rest of the network architectures. Within the tested concatenation schemes, *DDFFNet-CC1* and *DDFFNet-CC2* preserve most of the edges as expected, since they take extra information from the larger feature maps with still many details. In most of the cases though, too many edges are present in the disparity map, giving incorrect depth in some regions and therefore achieving overall worse MSE compared to that of *DDFFNet-CC3*. On the other hand, *DDFFNet-CC3* preserves only the most important edges which correspond to object boundaries. Going deeper in the concat connections would not provide sufficent fine structures, hence, we do not test connections after *CC3*.

DDFFNet-CC3 outperforms the other depth from focus method, *i.e*. VDFF [32], in all evaluation metrics, reducing depth error more than 70% and presents on-par results with depth from light-field approach.

Our method even matches the disparity MSE of Lytro, which uses the full grid of subaperture lens images to compute depth. Furthermore, as we can see in Figure 3, Lytro computes very inaccurate depth maps in terms of flat surfaces and creates artifacts on the results. On the other hand, *DDFFNet* estimates a smoother and also more accurate disparity maps. Quantitative results are presented in Table 2 and qualitative disparity comparisons are demonstrated in Figure 3.

Figure 7 illustrates the BadPix measure by changing the threshold τ. As one can see, DDFFNet-CC3 has a lower error by a large margin wrt VDFF. Moreover, we present

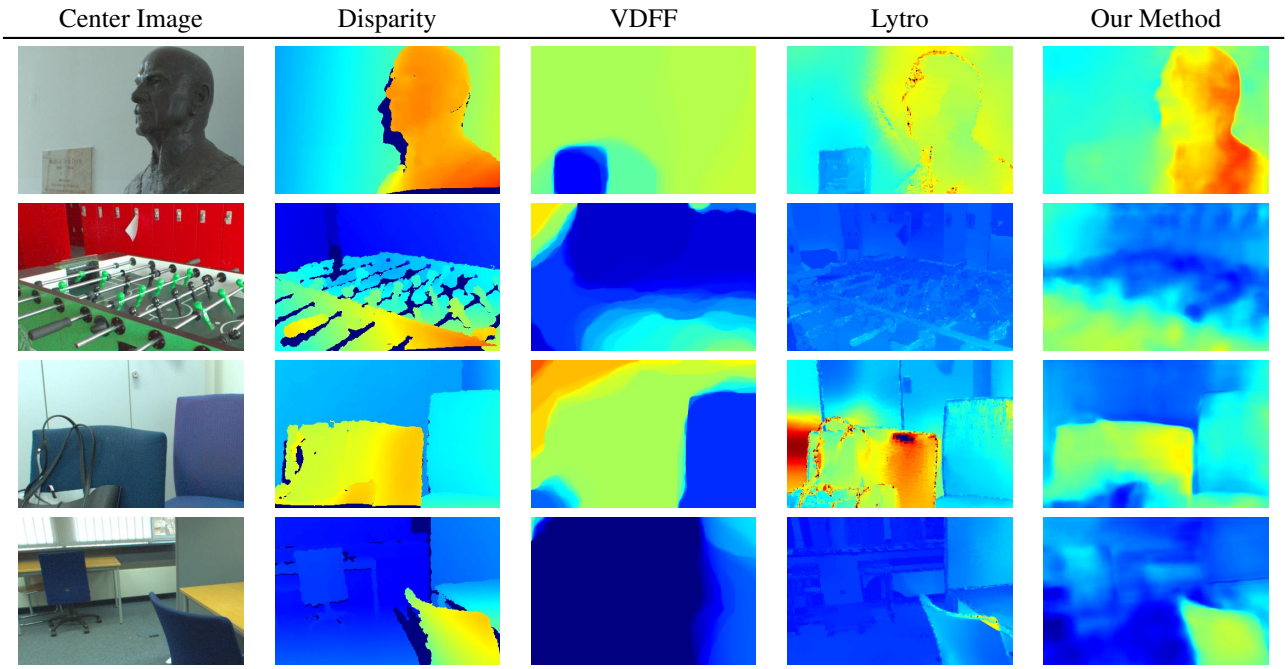

Figure 5. **Qualitative Results of DDFFNet versus state-of-the-art methods.** Results are normalized by the maximum disparity, which the focal stacks are generated on (0.28 pixel). Warmer colors represent closer distances. Best viewed in color.

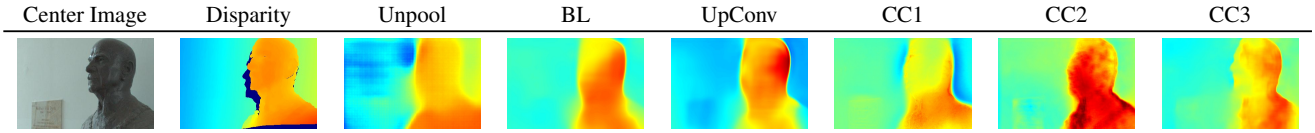

Figure 6. **Qualitative Results of variants of DDFFNet** While BL oversmooths the edges, CC1 and CC2 introduces artificial edges on the disparity map. Unpooling is not suitable well to smooth the flat surfaces while Best viewed in color.

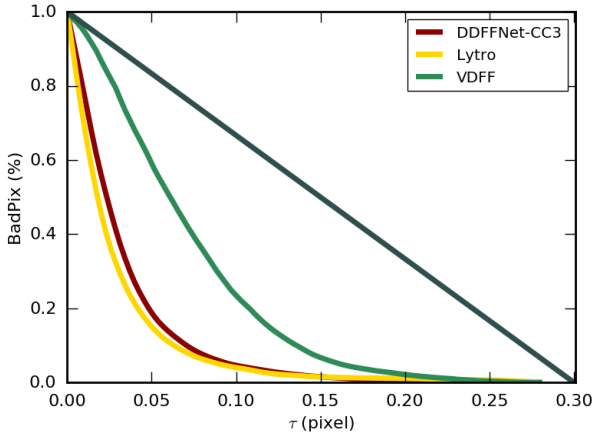

Figure 7. **Badpix(%)** for DDFFNet-CC3, Lytro and VDFF. While τ increases BadPix error decreases. DDFFNet is better than VDFF with a large margin and as good as Lytro.

the MSE and RMS errors computed on the predicted depth maps in Table 3. *DDFFNet-CC3* achieves the lowest error also on depth. Overall, experiments show that our method is more accurate by a large margin when compared to the classical variatonal DFF method [32], while being also orders of magnitude faster on a GPU. Several network architectures were explored, and finally CC3 was deemed the best with overall lowest disparity error while keeping object boundaries in the disparity map.

5. Conclusions

Depth From Focus (DFF) is a highly ill-posed inverse problem because the optimal focal distance is inferred from sharpness measures which fail in untextured areas. Existing variational solutions revert to spatial regularization to fill in the missing depth, but these typically do a poor job at representing more complex geometric environments. In this work, we proposed Deep Depth from Focus (DDFF) as the first deep learning solution to this classical inverse problem. To this end, we introduced a novel 30 times larger dataset with focal stacks from a light-field camera and ground truth depth maps from an RGB-D camera. We devised suitable network architectures, performed end-to-end training and demonstrated that DDFFNet outperforms existing approaches, reducing the depth error by more than 70% while being able to predict a disparity map in only 0.6 seconds.

References

[1] Lytro ILLUM lightfield camera. illum.lytro.com. Accessed: 2016-11-07. 3, 4, 6, 7

[2] M. Abadi, A. Agarwal, P. Barham, E. Brevdo, Z. Chen, C. Citro, G. S. Corrado, A. Davis, J. Dean, M. Devin, S. Ghemawat, I. Goodfellow, A. Harp, G. Irving, M. Isard, Y. Jia, R. Jozefowicz, L. Kaiser, M. Kudlur, J. Levenberg, D. Mané, R. Monga, S. Moore, D. Murray, C. Olah, M. Schuster, J. Shlens, B. Steiner, I. Sutskever, K. Talwar, P. Tucker, V. Vanhoucke, V. Vasudevan, F. Viégas, O. Vinyals, P. Warden, M. Wattenberg, M. Wicke, Y. Yu, and X. Zheng. TensorFlow: Large-scale machine learning on heterogeneous systems, 2015. Software available from tensorflow.org. 6

[3] E. Adelson and J. Wang. Tpami. In *Single lens stereo with a plenoptic camera*, 1992. 2

[4] M. Asif and T. Choi. Learning shape from focus using multilayer neural networks. In *Proc. SPIE, Vision Geometry VIII*, 1999. 2

[5] V. Badrinarayanan, A. Handa, and R. Cipolla. SegNet: A deep convolutional encoder-decoder architecture for robust semantic pixel-wise labelling. *arXiv preprint arXiv:1505.07293*, 2015. 1, 3

[6] Y. Bok, H.-G. Jeon, and I. S. Kweon. Geometric calibration of micro-lens-based light field cameras using line features. *PAMI*, 39(2):287–300, Feb 2017. 2, 4,

[7] D. Cho, M. Lee, S. Kim, and Y.-W. Tai. Modeling the calibration pipeline of the lytro camera for high quality light-field image reconstruction. In *ICCV*, 2013. 2

[8] D. Dansereau, O. Pizarro, and B. Williams. Decoding, calibration and rectification for lenselet-based plenoptic cameras. In *CVPR*, 2013. 2

[9] M. Diebold and B. Goldluecke. Epipolar Plane Image Refocusing for Improved Depth Estimation and Occlusion Handling. *Iccv*, 2013. 3

[10] A. Dosovitskiy, P. Fischer, E. Ilg, P. Häusser, C. Hazirbas, V. Golkov, P. van der Smagt, D. Cremers, and T. Brox. FlowNet: Learning Optical Flow with Convolutional Networks. In *ICCV*, Dec 2015. 1, 3, 5

[11] A. Dosovitskiy, J. Tobias Springenberg, and T. Brox. Learning to generate chairs with convolutional neural networks. In *CVPR*, June 2015. 5

[12] D. Eigen, C. Puhrsch, and R. Fergus. Depth map prediction from a single image using a multi-scale deep network. In *NIPS*, pages 2366–2374. 2014. 6

[13] S. Galliani and K. Schindler. Just look at the image: viewpoint-specific surface normal prediction for improved multi-view reconstruction. In *CVPR*, 2016. 3

[14] R. Garg, V. K. BG, and I. Reid. Unsupervised CNN for single view depth estimation: geometry to the rescue. In *ECCV*, 2016. 3, 6

[15] R. Girshick. Fast R-CNN. In *ICCV*, 2015. 3

[16] C. Hazirbas, L. Ma, C. Domokos, and D. Cremers. Fusenet: Incorporating depth into semantic segmentation via fusion-based cnn architecture. In *ACCV*, 2016. 1, 3

[17] K. He, X. Zhang, S. Ren, and J. Sun. Delving deep into rectifiers: Surpassing human-level performance on imagenet classification. In *ICCV*, 2015. 6

[18] K. He, X. Zhang, S. Ren, and J. Sun. Deep residual learning for image recognition. In *CVPR*, 2016. 3, 5

[19] K. Honauer, O. Johannsen, D. Kondermann, and B. Goldluecke. A dataset and evaluation methodology for depth estimation on 4d light fields. In *ACCV*, 2016. 3, 5, 6

[20] S. Ioffe and C. Szegedy. Batch normalization: Accelerating deep network training by reducing internal covariate shift. volume 37 of *JMLR Proceedings*, pages 448–456. JMLR.org, 2015. 5

[21] H.-G. Jeon, J. Park, G. Choe, J. Park, Y. Bok, Y.-W. Tai, and I. S. Kweon. Accurate depth map estimation from a lenslet light field camera. In *CVPR*, 2015. 2, 3

[22] A. Kendall, V. Badrinarayanan, and R. Cipolla. Bayesian SegNet: Model uncertainty in deep convolutional encoder-decoder architectures for scene understanding. *arXiv preprint arXiv:1511.02680*, 2015. 3, 5

[23] A. Kendall, M. Grimes, and R. Cipolla. Posenet: A convolutional network for real-time 6-dof camera relocalization. In *ICCV*, 2015. 3

[24] A. Krizhevsky, I. Sutskever, and G. E. Hinton. Imagenet classification with deep convolutional neural networks. In *NIPS*, 2012. 3, 5

[25] B. Li, C. Shen, Y. Dai, A. van den Hengel, and M. He. Depth and surface normal estimation from monocular images using regression on deep features and hierarchical crfs. In *CVPR*, 2015. 3

[26] H. Lin, C. Chen, S. B. Kang, and J. Yu. Depth recovery from light field using focal stack symmetry. In *ICCV*, 2015. 2

[27] F. Liu, C. Shen, G. Lin, and I. D. Reid. Learning depth from single monocular images using deep convolutional neural fields. *PAMI*, 38(10):2024–2039, 2016. 6

[28] M. Y. Liu, O. Tuzel, and Y. Taguchi. Joint geodesic upsampling of depth images. In *CVPR*, June 2013. 4

[29] J. Long, E. Shelhamer, and T. Darrell. Fully convolutional networks for semantic segmentation. In *CVPR*, pages 3431–3440, Boston, MA, USA, June 2015. IEEE. 1, 3, 5

[30] M. Mahmood. Shape from focus by total variation. In *Proc. IEEE, 11th IVMSP Workshop*, 2013. 2

[31] M. Mahmood and T.-S. Choi. Nonlinear approach for enhancement of image focus volume in shape from focus. In *IEEE Trans. Image Process.*, 2012. 2

[32] M. Moeller, M. Benning, C. Schönlieb, and D. Cremers. Variational depth from focus reconstruction. *IEEE Transactions on Image Processing*, 24(12):5369–5378, Dec 2015. 2, 6, 7, 8

[33] R. Ng, M. Levoy, M. Brédif, G. Duval, M. Horowitz, and P. Hanrahan. Light field photography with a hand-held plenoptic camera. Technical report, Stanford, 2005. 2

[34] N.Mayer, E.Ilg, P.Häusser, P.Fischer, D.Cremers, A.Dosovitskiy, and T.Brox. A large dataset to train convolutional networks for disparity, optical flow, and scene flow estimation. In *IEEE International Conference on Computer Vision and Pattern Recognition (CVPR)*, 2016. arXiv:1512.02134. 1, 3, 5

[35] H. Noh, S. Hong, and B. Han. Learning deconvolution network for semantic segmentation. *ICCV*, 2015. 1, 3, 5

[36] J. Park, H. Kim, Y. Tai, M. S. Brown, and I. Kweon. High-quality depth map upsampling and completion for RGB-D cameras. *IEEE Trans. Image Processing*, 2014. 4

[37] J. Park, H. Kim, Y.-W. Tai, M. S. Brown, and I. Kweon. High quality depth map upsampling for 3d-tof cameras. In *ICCV*, Nov 2011. 4

[38] F. Pérez-Nava and J. P. Lüke. Simultaneous estimation of super-resolved depth and all-in-focus images from a plenoptic camera. In *3DTV Conference: The True Vision - Capture, Transmission and Display of 3D Video*, 2009. 2

[39] S. Pertuz, D. Puig, and M. A. Garcia. Analysis of focus measure operators for shape-from-focus. *Pattern Recognition*, 46(5):1415–1432, May 2013. 2

[40] O. Russakovsky, J. Deng, H. Su, J. Krause, S. Satheesh, S. Ma, Z. Huang, A. Karpathy, A. Khosla, M. Bernstein, A. C. Berg, and L. Fei-Fei. ImageNet Large Scale Visual Recognition Challenge. *IJCV*, 115(3):211–252, 2015. 3

[41] J. Shen and S. C. S. Cheung. Layer depth denoising and completion for structured-light rgb-d cameras. In *CVPR*, June 2013. 4

[42] K. Simonyan and A. Zisserman. Very deep convolutional networks for large-scale image recognition. 2015. 3, 5

[43] S. Suwajanakorn, C. Hernandez, and S. M. Seitz. Depth from focus with your mobile phone. In *CVPR*, pages 3497–3506, June 2015. 2

[44] A. Thelen, S. Frey, S. Hirsch, and P. Hering. Improvements in shape-from-focus for holographic reconstructions with regard to focus operators, neighborhood-size, and height value interpolation. In *IEEE Trans Image Process.*, 2009. 2

[45] S. Wanner, S. Meister, and B. Goldlücke. Datasets and benchmarks for densely sampled 4d light fields. In *VMV*, pages 225–226, 2013. 3, 5

[46] B. Wilburn, N. Joshi, V. Vaish, E. Talvala, E. Antunez, A. Barth, A. Adams, M. Horowitz, and M. Levoy. Acm transactions on graphics. In *High performance imaging using large camera arrays*, 2005. 2

Deep Depth From Focus
Supplementary Material

Abstract

In this supplementary material we include additional information for the reader. We first detail the formulation of the light-field calibration and provide the values for all parameters. We then detail the characteristics of the new DDFF 12-Scene dataset, such as disparity histograms per sequence and disparity sampling. Finally, we present more qualitative results including the failure cases and also visualizations of the activation heat maps for our best performing model, i.e. *DDFFNetCC3.*

1. Light-field Camera Calibration

We make use of the light-field camera calibration toolbox by Bok *et al*. [6], which generates the subapertures based on a *radius* r_m of a microlens image, which is set to 7 pixels for Lytro ILLUM camera. Although the toolbox generates 13×13 subapertures, we follow the authors recommendation [6] to only use the subapertures within the displacement $i^2 + j^2 < (radius - 1)^2$. This results in 9×9 subapertures. Estimated intrinsic parameters of the LYTRO Illum are given in Table 1. Intrinsics of the microlenses are computed as

$$\text{Int} = \begin{bmatrix} F_x/(2r_m) & 0 & C_x/(2r_m) \\ 0 & F_x/(2r_m) & C_y/(2r_m) \\ 0 & 0 & 1 \end{bmatrix}. \quad (1)$$

Table 1. **Estimated intrinsics** parameters of the LYTRO Illum. F_* and C_* are respectively the focal length and optical center of the main lens in pixels. Baseline (K_1/F') is the distance between two adjacent subapertures in meter/pixel, where $F' = \max(F_x, F_y)$. Refer to [6] for details.

Parameters	Lytro Illum	Parameters	Lytro Illum
r_m	7	F_x	7299.7
K_1	-2.768	F_y	7317.0
K_2	1982.0	C_x	3991.6
k_1	0.388	C_y	2629.6
k_2	-0.0361	K_1/F'	27e−5

2. DDFF 12-Scene Dataset

Our new dataset is composed of 12 scenes. We use as training set the first six scenes with 100 light-field samples each, for a total of 600 light-field training images. The other 6 scenes have 20 light-field samples each and are used for testing. All 720 light-field images have registered ground truth depth/disparity maps obtained from an RGB-D sensor.

In Figure 1, the disparity distribution of the twelve scenes is shown. In Figure 2, we plot the normalized disparity histogram of the training and test sets. We generate the focal stacks for 10 sampled disparities in the interval of $[0.28, 0.02]$ pixels (equivalent to $[0.5, 7]$ meters), indicated with blue dashed lines in Figure 2a. We also plot the depth to disparity conversion for the given baseline and focal length of the microlenses in Figure 2b. Refocused disparity values and their corresponding depths are denoted with a green box. Note that disparity is inversely proportional to depth and therefore linear sampling in disparity corresponds to non-linear sampling in depth. We choose to sample disparities to have a linear focus change between stack images.

3. DDFFNet results

We present further qualitative results in Figure 3. Note the poor performance of classic methods like VDFF, and even the wrong disparity maps produced by Lytro in the first row. In Figure 4 we present two failure cases where the network output is not sharp or not consistent. Furthermore, we show the activation heat maps for three focal stacks in Figure 5. The network outputs an activation stack before the *score* layer, see Figure 2 in the manuscript. Note how each activation map favors different parts of the image depending on their depth, suggesting the network indeed learns the relationship between depth and an input image of the focal stack, hence performing depth-from-focus.

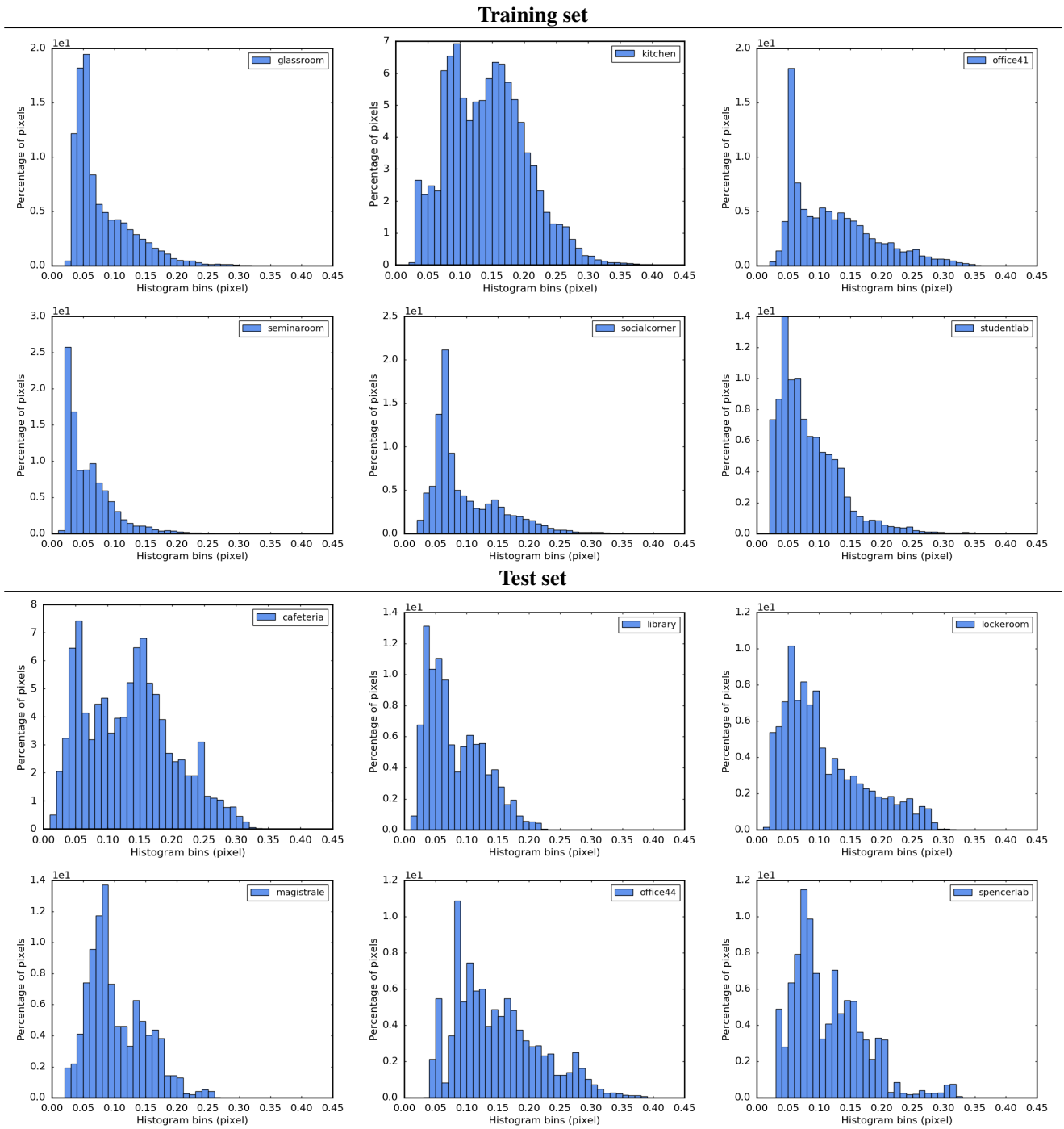

Figure 1. **Disparity distribution** of the DDFF 12-Scene dataset. Each of the first 6 scenes is composed of 100 light-field samples and used for training. Each of the latter 6 scenes is composed of 20 light-field samples and used for testing.

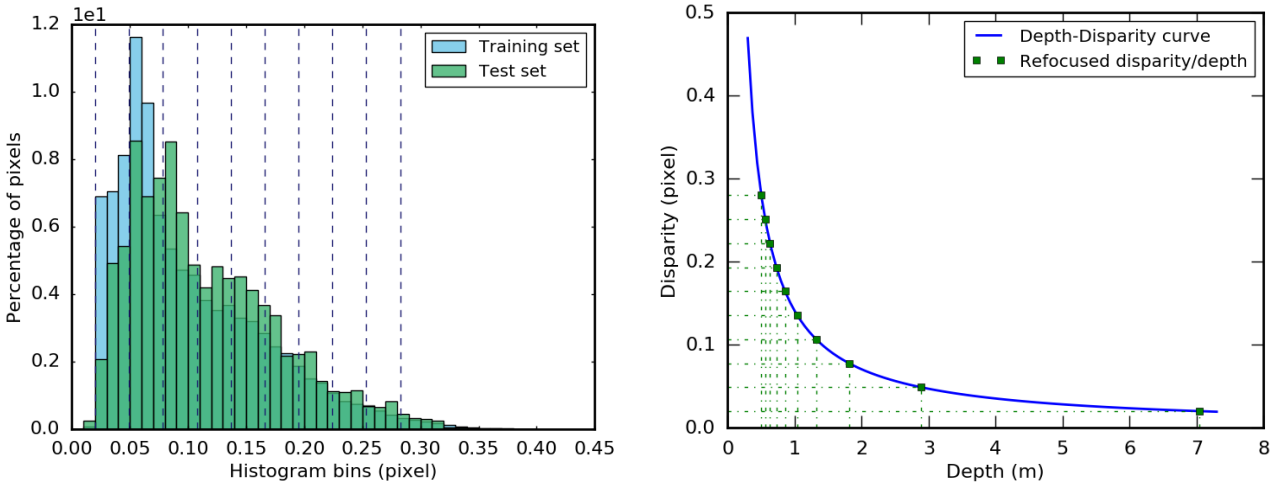

(a) (b)

Figure 2. (a) **Disparity Distribution** of the training and test sets. Dashed blue lines represent the sampled disparity values used to generate the focal stacks. (b) **Depth to disparity** conversion for DDFF 12-Scene dataset. Sampled disparities used for refocusing and their corresponding depths are denoted with green boxes.

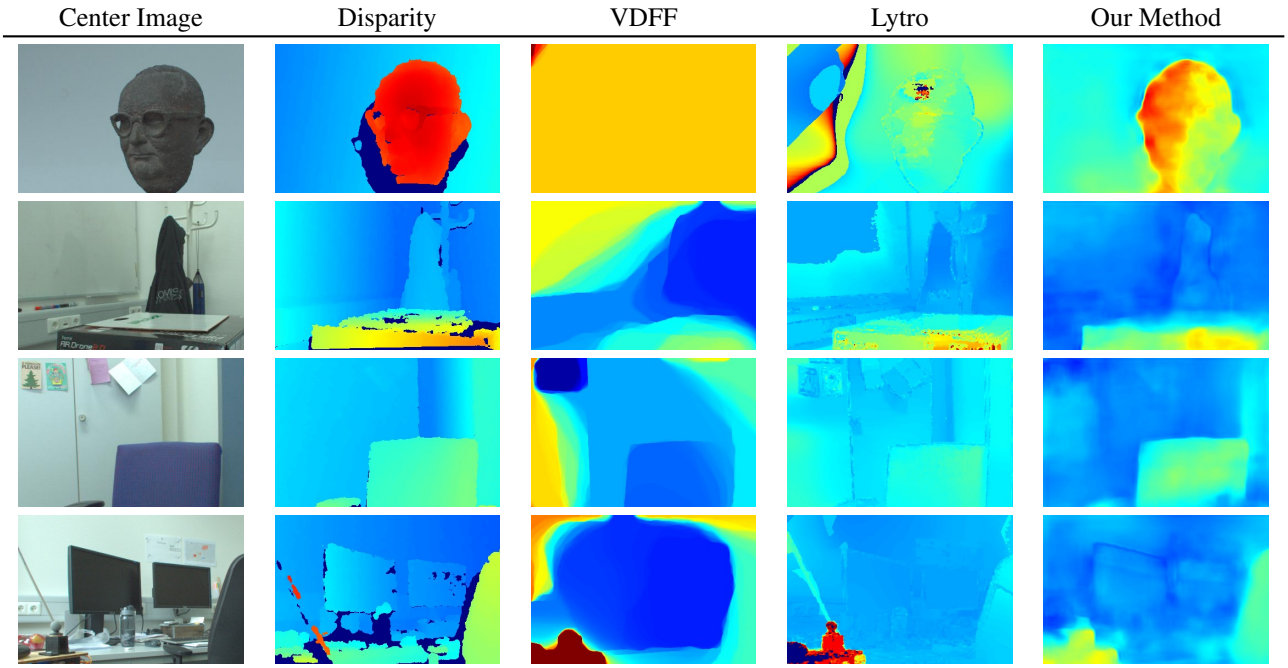

Figure 3. **Qualitative Results of DDFFNet versus state-of-the-art methods.** Results are normalized by the maximum disparity. Warmer colors represent closer distances. Best viewed in color.

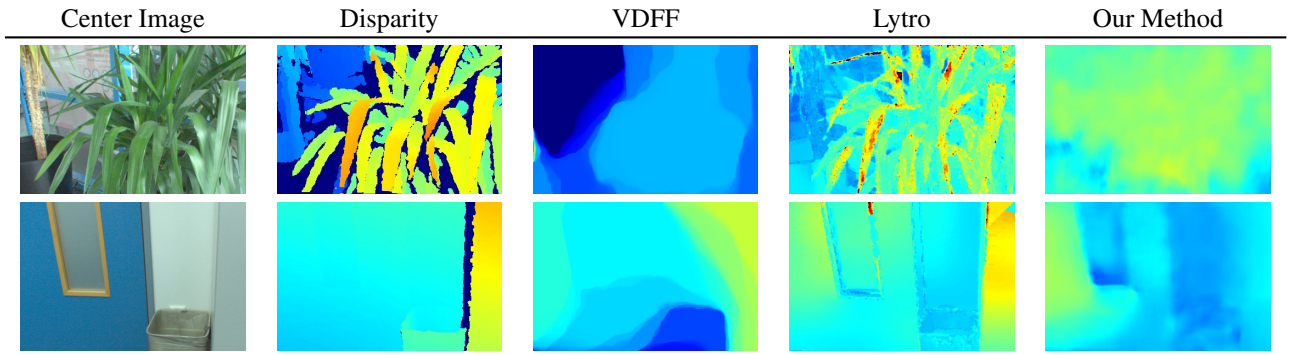

Figure 4. **Failure cases.** Results are normalized by the maximum disparity. Warmer colors represent closer distances. Best viewed in color.

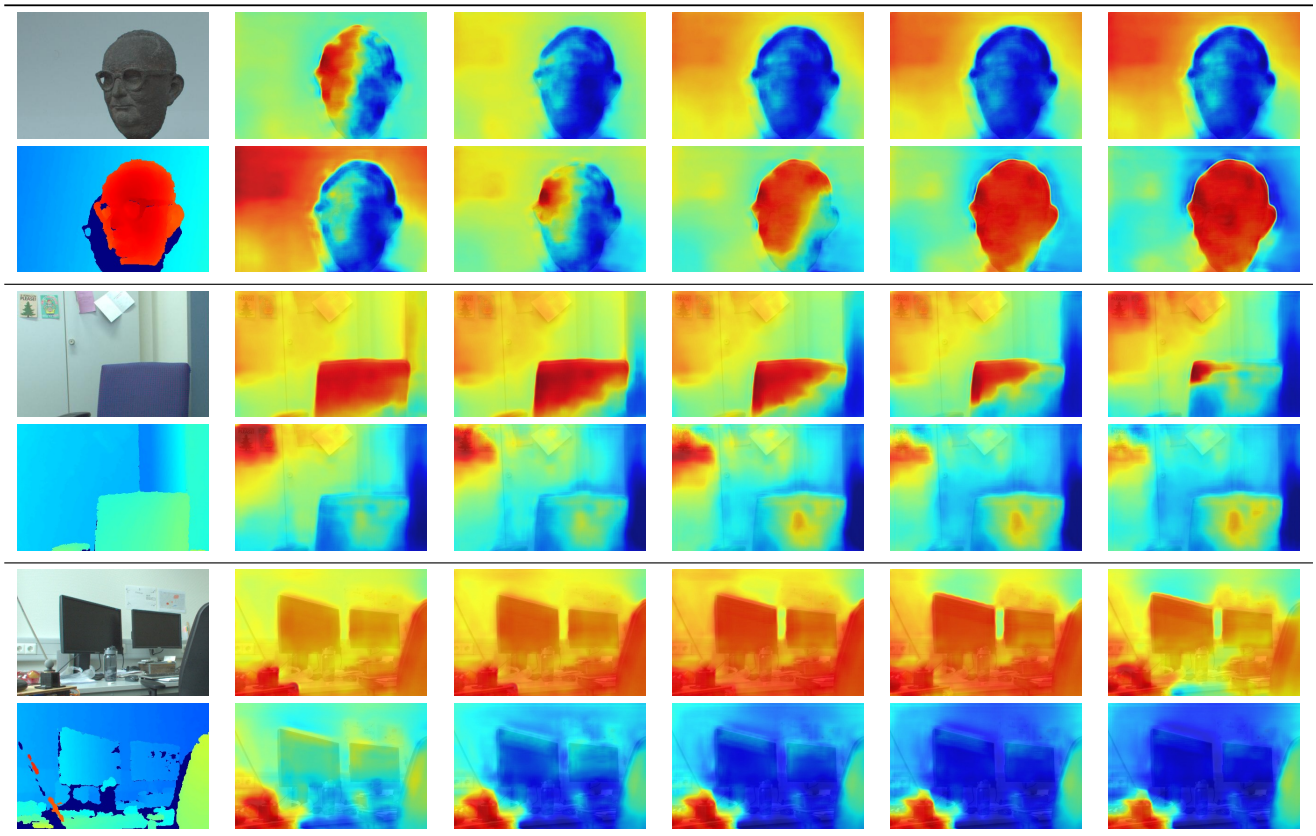

Figure 5. **Activation heat maps** for the refocused images in a focal stack. First column shows the center subaperture image and its corresponding ground truth disparity map. Rest of the columns from left to right, top to bottom demonstrate the activation on the refocused images. Heat maps are overlaid with the center image and warmer colors represent higher activations.